AIMS Mathematics

AIMS Mathematics, 11(4): 10226–10256.
DOI: 10.3934/math.2026423
Received: 13 December 2025
Revised: 26 February 2026
Accepted: 09 March 2026
Published: 15 April 2026

http://www.aimspress.com/journal/Math

Research article

Hybrid PINN-IFE approach for solving transmission problems in circular interface domains

Muhammad Azam[1], **Dalal Alhwikem**[2,*] **and Naseer Ullah**[1]

[1] Key Laboratory of Urban Security and Disaster Engineering of the Ministry of Education, Beijing University of Technology, Beijing 100124, China
[2] Department of Mathematics, College of Science, Qassim University, Buraydah 52571, Saudi Arabia

* **Correspondence:** Email: d.alhwikem@qu.edu.sa.

Abstract: In this study, we proposed a hybrid methodology combining Physics-Informed Neural Networks (PINNs) and Immersed Finite Element (IFE) methods to address transmission problems in complex geometries, with a focus on Helmholtz-type equations. The technique addressed the challenge of solving wave equations in domains with circular interfaces, where material properties differ across the interface. The hybrid model leverages the strengths of PINNs to enforce the governing physical equations and IFE to provide a coarse initial solution, which is then corrected by the neural network using a signed-distance function to the interface. This correction was trained on a combination of supervised loss from data, physics-informed residual predictions, and interface conditions. Numerical experiments demonstrated high precision of the proposed technique when compared with manufactured exact solutions, achieving low error levels in both subdomains. High-frequency tests at $\omega = 100$ further validated the method's accuracy and robustness across material configurations including normal and inverted contrast cases. Its mesh-free character provides flexibility and versatility for a wide range of transmission problems in computational physics, making it a promising method for solving interface-related issues in wave propagation.

Keywords: physics-informed neural networks (PINNs); interface problems; hybrid methods; machine learning; transmission problems; wave propagation

1. Introduction

The propagation of waves in composite media of various materials has applications in a wide range of fields in science and engineering; for example, wave diffraction [1,2], wave scattering [3], and wave reflection and transmission [4,5], to mention only a few. In an appropriate physical regime, the amplitude of the wave is described by the Helmholtz equation. Moreover, the amplitude must satisfy the jump conditions [6] across the interface between any two types of materials, imposed by the requirements of the relevant physics, including continuity of the pressure [4], the normal velocity [5], and the volume flow [7]. Interface-free Helmholtz boundary value problems (BVPs) have been extensively treated numerically using classical finite element methods. Interface-free Helmholtz boundary value problems (BVPs) have been extensively treated numerically using classical finite element methods. Brown [8] analyzed the numerical solution of the wave equation with piecewise smooth coefficients. Kreiss and Petersson [9] developed an embedded boundary method for the wave equation with discontinuous coefficients. Aziz and Werschulz [10] studied the numerical solutions of Helmholtz's equation by the finite element method. Babuška and Sauter [11] investigated the pollution effect of the FEM for the Helmholtz equation considering high wave numbers. Douglas, Sheen, and Santos [12] presented an approximation of scalar waves in the space-frequency domain. Ihlenburg and Babuška [13] examined the finite element solution of the Helmholtz equation with high wave number focusing on the h-version of the FEM. More advanced finite element schemes have also been developed for solving Helmholtz boundary value problems. Burman, Wu, and Zhu [14] developed a linear continuous interior penalty finite element method for the Helmholtz equation with high wave number. Du and Wu [15] presented a preasymptotic error analysis of higher order FEM and CIP-FEM for the Helmholtz equation with high wave number. Farhat, Harari, and Hetmaniuk [16] introduced a discontinuous Galerkin method with Lagrange multipliers for Helmholtz problems in the mid-frequency regime. Feng and Wu [17] analyzed discontinuous Galerkin methods for the Helmholtz equation with large wave numbers. Gittelson, Hiptmair, and Perugia [18] presented a plane wave discontinuous Galerkin method with analysis of the h-version. Lam and Shu [19] developed a phase-based interior penalty discontinuous Galerkin method for the Helmholtz equation with spatially varying wavenumber. Melenk, Parsania, and Sauter [20] proposed general DG methods for highly indefinite Helmholtz problems.

The methods described above, i.e., finite element methods, can be employed to solve interface problems, as long as they employ a body-fitting mesh, i.e., where each element lies entirely on one side of the interface. This body-fitting requirement may be problematic in situations where an interface problem must be solved on multiple, and often different, geometries and where complete mesh regeneration is required for each instance. Interface-independent meshing can also be advantageous in the numerical techniques used for such simulations. To this end, methods have been proposed for elliptic PDEs where the mesh is independent of the interface, including extended finite element methods (X-FEM) [21], unfitted finite element methods [22], multi-scale methods [23], and immersed interface methods (IIM) [24,25]. Some of these have been applied to Helmholtz interface problems, with IIM and X-FEM implementations discussed in [6].

Another type of finite element methods that enable interface-independent meshing is the immersed finite element (IFE) methods. By using Hsieh-Clough-Tocher type macro polynomials [26] that have interface jump conditions as the local shape functions, IFE methods can use highly structured Cartesian meshes to discretize problems with a non-trivial interface. IFE spaces based on triangular

Cartesian meshes have been developed and analyzed in several works [27–29], while those based on rectangular Cartesian meshes are discussed in [30,31]. Discontinuous Galerkin IFE (DGIFE) methods [32,33] and partially penalized IFE (PPIFE) methods [34,35] have since been developed to address elliptic interface problems, with generalizations to higher-degree approximations in [36].

Physics-Informed Neural Networks (PINNs), originally introduced by Raissi et al. [37], have emerged as a powerful paradigm for solving partial differential equations by embedding physical laws directly into the neural network loss function. Subsequent advancements have extended PINNs to handle increasingly complex problems, including understanding gradient flow pathologies [38], solving frequency-domain Helmholtz problems [39], handling interface and free boundary problems [40], making advances in physics-informed machine learning [41], and adapting PINN methods [42]. In particular, specialized architectures have been developed for Helmholtz-type equations to address challenges such as spectral bias and pollution effects, including stabilized PINNs [43], PINN variants and applications [44], and multi-level optimization approaches. In this work, we build upon these foundations by integrating PINNs with IFE methods to leverage the strengths of both approaches.

Here, we report on a new hybrid Physics-Informed Neural Network - Immersed Finite Element (PINN-IFE) that addresses the Helmholtz interface problem modeled by Eqs (1) and (2) as a PINN and (3) and (4) as an IFE. The Helmholtz equation satisfies the same interface jump conditions (3) and (4) as the elliptic interface problems and, thus, we take advantage of IFE methods to build a robust baseline solution that automatically satisfies interface conditions in a structured cartesian mesh. Nevertheless, to address this drawback of the classical IFE approaches (i.e., pollution effect and numerical dispersion at large wave numbers [45]), we enhance the IFE solution with a physics-informed neural network (PINN) [37]. This combination technique is designed, with the IFE solution serving as a prior, which enables the PINN to learn a high-fidelity correction term, so that in addition to the structured efficiency of IFE, this method has the adaptive and mesh free power of deep learning. Advances in numerical methods for Helmholtz-type equations have demonstrated high accuracy, achieving errors of 10^{-4} to 10^{-5} for wave number ω=100 [44].

This hybrid paradigm offers several advantages: The interface conditions are enforced using the IFE basis, and the absorbing boundary condition (2) is explicitly implemented into the loss function, and the approximation power of the neural network is utilized to lower the errors at the interface and at large wave numbers. Moreover, it can be very accurate, with few degrees of freedom, with a correction to a coarse IFE solution, and it is efficient on high wave number problems. Nevertheless, it should be mentioned that the method has not been validated in circular interfaces, and its performance is affected by the manual tuning of the loss weights. Additionally, the computational cost and its ability to scale to 3D problems have not been quantified.

Moreover, although interfacial discontinuities can be modeled using IFE methods, the numerically demanding nature of satisfying flux continuity conditions across high-ratio interfaces (e.g., $\beta_1,\ \beta_2 = 50$) can be computationally expensive. The hybrid PINN-IFE scheme presented below is meant to address these limitations by exploiting the mesh-free adaptability of neural networks to amend the inaccurate IFE solution, thus improving accuracy with the corresponding reduction in computational cost of overly fine mesh refinement.

2. Problem statements

In this study, we focus on solving Helmholtz-type transmission problems within a domain that contains a material interface. Wave propagation in such composite media, where abrupt changes of physical properties occur at an interface, is fundamental to applications in acoustics and electromagnetics. The fundamental problem is to compute the wave field while satisfying the governing equations within each subdomain, the jump conditions at the interface, and the far field radiation condition.

Consider a bounded computational domain $\Omega \in R^2$, which is divided by a smooth, closed circular interface Γ into two subdomains: An interior Ω^1 and exterior Ω^2, such that $\Omega = \Omega^1 \cup \Omega^2 \cup \Gamma$.

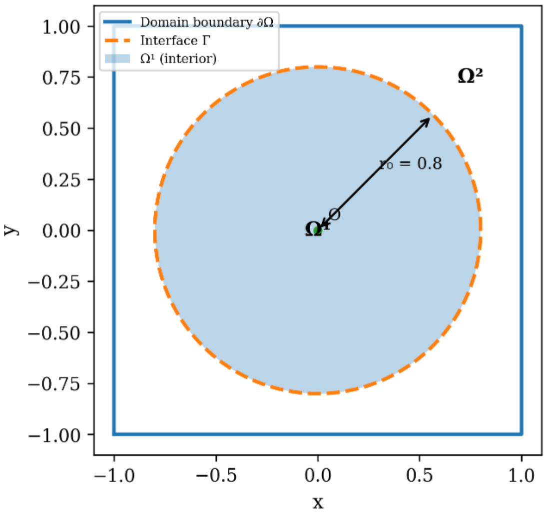

Figure 1. Computational domain with circular interface Γ (radius $r_0 \approx 0.8$).

The interface is defined by $\Gamma = \{(x,y) \mid x^2 + y^2 = r_0^2\}$, with radius r_0.

The problem is to find a complex-valued wave field $u(X)$, for $X = (x,y) \in \Omega$, that satisfies the following set of equations:

2.1. Governing PDE

The Helmholtz equation with piecewise-constant coefficients holds throughout the domain, except at the interface:

$$\nabla \cdot (\beta \nabla u) + \omega^2 u + f = 0 \text{ in } \Omega^1 \cup \Omega^2, \tag{1}$$

where ω is the wave number, f is a source term, and $\beta(X)$ is the material parameter defined as:

$$\beta(X) = \begin{cases} \beta_1, \forall X \in \Omega^1, \\ \beta_2, \forall X \in \Omega^2. \end{cases} \tag{1a}$$

A significant contrast between β_1 and $\beta_2 (e.g., \beta_1 = 1, \beta_2 = 50)$ presents a primary numerical challenge.

2.2. Boundary conditions

On the outer boundary $\partial\Omega$, , a first order absorbing boundary condition is imposed to approximate the radiation condition for outgoing waves:

$$\beta \frac{\partial u}{\partial n_\Omega} + i\omega u = g \text{ on } \partial\Omega, \tag{2}$$

where n_Ω is the unit outward normal to $\partial\Omega, i = \sqrt{-1},$ and g is a known function.

2.3. Interface jump conditions

The solution should impose continuity of the field and flux across the interface in the material Γ.

$$[u]_\Gamma := u^1 |_\Gamma - u^2 |_\Gamma = 0 \text{ (Continuity of Solution)}, \tag{3}$$

$$[\beta \nabla u \cdot n]_\Gamma := \beta_1 \nabla u^1 \cdot n |_\Gamma - \beta_2 \nabla u^2 \cdot n |_\Gamma = 0 \text{ (Continuity of Flux)} \tag{4}$$

where n is the unit normal vector on Γ, and $u^s = u|_{\Omega^s}$ for $s = 1, 2.$

The material property $\beta(X)$ is a piecewise constant function, characterized by a potentially high contrast across the interface, as shown in Eq (1a).

Since the Helmholtz equation represents time-harmonic wave fields, it is a boundary value problem, and initial conditions are not possible. The main difficulty is to solve the problem with accurate resolution in the high wave numbers (ω) and large material contrasts (β_2 / β_1), which are the hallmarks of this problem, addressing the pollution errors and inefficiency of conventional interface fitted and immersed schemes.

3. The hybrid PINN-IFE framework

In this section, we delineate the core innovation of this work: A synthesis of the structural capabilities of Immersed Finite Elements (IFE) on the one hand and the capabilities of Physics-Informed Neural Network (PINNs) to generalize to all approximations on the other hand. The approach is based on a functional decomposition of the solution in which the IFE component identifies the interface constraints, and the PINN identifies a corrective field to achieve high-frequency accuracy and minimize the numerical dispersion, which is most important when high wave numbers are used.

The overall architecture of the framework is illustrated in Figure 2, which outlines the integrated workflow from problem definition to the final high-fidelity solution.

3.1. Solution decomposition and network architecture

The hybrid solution u_{hybrid} is formulated through an additive composition of a computable baseline and a neural network-based:

$$u_{hybrid} = u_{ife} + u_{corr}. \tag{5}$$

3.1.1. The IFE Baseline (u_{ife})

The term $u_{ife} \in S_h^k(\Omega)$ is the numerical solution obtained from the Partially Penalized IFE (PPIFE) method on a coarse Cartesian mesh. This baseline solution is computationally efficient to obtain and, by construction, satisfies the interface jump conditions (3) and (4) in a weak sense. Its fundamental purpose is to resolve the global structure of the solution and the discontinuous gradient across the interface, providing a robust prior that encapsulates the essential physics of the transmission problem.

3.1.2. The PINN (u_{corr})

The correction term u_{corr} is the output of a deep neural network N_Θ that is sensitized to the interface geometry. The network maps spatial coordinates and a geometric hint to the corrective field:

$$u_{corr}(X) = N_\Theta(X, \phi(X)), \tag{6}$$

where $\phi(X) = \|X\| - r_0$ is the signed distance function (SDF) from the interface Γ. The incorporation of the SDF is a critical innovation, as it explicitly informs the network of the precise interface location, enabling it to learn sharp and precise corrective adjustments in the vicinity of Γ without necessitating excessive point sampling or network capacity. The network is a multi-layer perceptron (MLP) with five hidden layers each containing 20 neurons employing the hyperbolic tangent ($tanh$) activation function. The output layer is linear with two neurons, representing the real and imaginary parts of the complex-valued correction $\hat{u}(x, y)$. "$Tanh$" is selected instead of sinusoidal activations since it offers stable gradients on the second-order derivatives occurring in the Helmholtz residual, especially on high wave numbers, where sinusoidal activations are unstable to training. The parameters Θ encompass the weights and biases of the network. The final output layer is linear and consists of two neurons, representing the real and imaginary parts of the complex-valued correction u_{corr}.

$Tanh$ is selected instead of sinusoidal activations since it offers stable gradients on the second-order derivatives occurring in the Helmholtz residual, especially on high wave numbers, where sinusoidal activations are unstable to training. Additionally, tanh is preferred because its bounded output $[-1, 1]$ prevents activation blow-up during training, and it has been extensively validated in PINN literature for wave propagation problems. In all numerical experiments presented in this work, tanh activation is used exclusively due to its superior stability and accuracy for high wave number problems.

3.2. The composite physics-informed loss function

The parameters Θ of the network are optimized by minimizing a composite, weighted loss function $J(\Theta)$ that ensures the hybrid solution satisfies the governing physics and remains consistent with the IFE baseline:

$$J(\Theta) = \lambda_{pde} L_{pde} + \lambda_{\text{int}erface} L_{\text{int}erface} + \lambda_{data} L_{data}. \tag{7}$$

The weighting coefficients in Eq (7) are set to $\lambda_{\text{pde}} = 1.0$, $\lambda_{\text{interface}} = 10.0$, $\lambda_{\text{bc}} = 5.0$, and $\lambda_{\text{data}} = 1.0$ for all numerical examples. These values remain constant throughout training; no annealing or scheduling is employed. The interface term is weighted highest to ensure accurate satisfaction of the jump conditions, followed by the boundary term to properly enforce the absorbing condition.

3.2.1. PDE Residual Loss (L_{pde})

This term enforces the Helmholtz equation (1) throughout the domain. Let $X_{pde} \subset \Omega$ be a

quasi-uniformly distributed set of collocation points. The loss is defined as the mean squared error of the PDE residual:

$$L_{pde} = \frac{1}{N_{pde}} \sum_{X_i \in X_{pde}} \left| -\nabla \cdot \left(\beta \nabla u_{hybrid} \right) - \omega^2 u_{hybrid} - f \right|^2 (X_i). \tag{8}$$

The required derivatives of u_{hybrid} are computed via automatic differentiation, a powerful feature of the PINN framework that avoids discretization error.

Sampling strategy near the interface. To avoid evaluating the strong form of the PDE at points where the material coefficient β is discontinuous, we explicitly exclude a narrow neighborhood around the interface Γ when selecting PDE collocation points. Let $\mathcal{N}_\delta(\Gamma) = \{X \in \Omega\text{:dist}(X, \Gamma) < \delta\}$ denote an exclusion zone of width δ on either side of the interface. Collocation points are sampled from $\Omega^1 \setminus \mathcal{N}_\delta(\Gamma)$ and $\Omega^2 \setminus \mathcal{N}_\delta(\Gamma)$, ensuring that the PDE residual is evaluated only in regions where β is constant and the classical derivatives are well-defined. Within $\mathcal{N}_\delta(\Gamma)$, the physics is enforced exclusively through the interface loss term $L_{interface}$ defined in Eqs (9)–(11).

The exclusion width δ is chosen to scale linearly with the IFE mesh size h as $\delta = \alpha h$, with $\alpha = 0.1$ in all numerical experiments. This scaling ensures that as the mesh is refined, the excluded region shrinks proportionally, maintaining consistency with the overall convergence of the method. The choice of α is empirical and balances the need to avoid the discontinuity while preserving sufficient sampling density near the interface. A sensitivity study confirmed that results are stable for $\alpha \in [0.05, 0.2]$.

3.2.2. Interface condition loss $\left(L_{interface}\right)$

This term guarantees the exact enforcement of the jump conditions across the interface.

Let X_Γ^+ and X_Γ^- be sample points taken on opposite sides of the interface along the normal direction. The loss comprises two components:

$$L_{interface} = L_{continuity} + L_{flux}, \tag{9}$$

$$L_{continuity} = \frac{1}{N_\Gamma}\sum_j \left|u_{hybrid}(X_j^+) - u_{hybrid}(X_j^-)\right|^2, \tag{10}$$

$$L_{flux} = \frac{1}{N_\Gamma}\sum_j \left|\beta_2 \nabla u_{hybrid}\left(X_j^+\right)\cdot n - \beta_1 \nabla u_{hybrid}\left(X_j^-\right)\cdot n\right|^2. \tag{11}$$

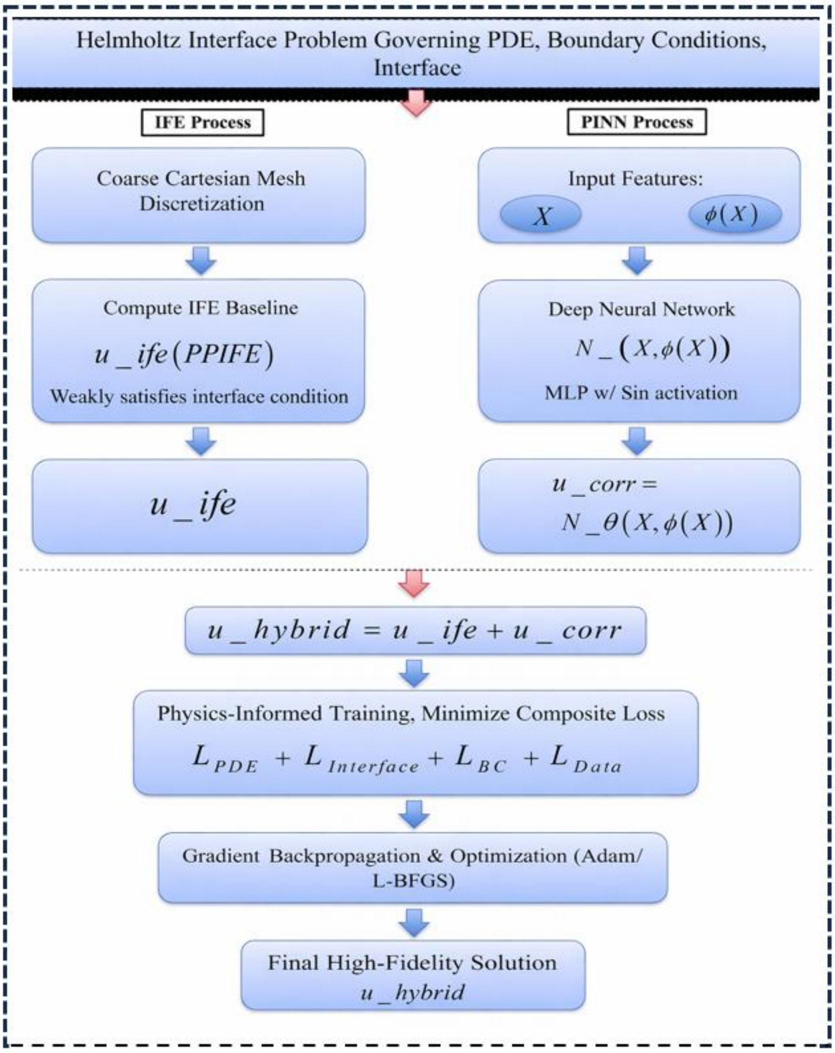

Figure 2. Hybrid methodology combining IFE and PINN for solving Helmholtz interface.

3.2.3. Boundary condition loss (L_{bc})

This term enforces the first-order absorbing boundary condition (2) on the domain boundary $\partial\Omega$:

$$L_{bc} = \frac{1}{N_{bc}} \sum_{X_k \in X_{bc}} \left| \beta \frac{\partial u_{hybrid}}{\partial n_\Omega} + i\omega u_{hybrid} - g \right|^2 (X_k). \tag{12}$$

3.2.4. Boundary condition loss (L_{bc})

This supervised component anchors the PINN to the coarse IFE solution, providing a baseline for the correction:

$$L_{data} = \frac{1}{N_{data}} \sum_{i=1}^{N_{data}} \left| u_{hybrid}(X_i) - u_{IFE}(X_i) \right|^2. \tag{13}$$

3.2.5. Treatment of complex-valued quantities

Since the Helmholtz equation involves complex-valued wave fields, special care is taken in formulating the loss function. In our framework, all complex quantities are decomposed into their real and imaginary components. The neural network N_Θ is designed with two output neurons corresponding to $\Re(u_{corr})$ and $\Im(u_{corr})$, respectively. Consequently, the hybrid solution is expressed as $u_{hybrid} = (\Re(u_{ife}) + \Re(u_{corr})) + i(\Im(u_{ife}) + \Im(u_{corr}))$.

For each physical constraint, we compute separate loss terms for the real and imaginary parts and sum them, rather than minimizing the squared magnitude of the complex residual. For instance, the PDE residual loss L_{pde} in Eq (8) is implemented as:

$$L_{pde} = \frac{1}{N_{pde}} \sum_{i=1}^{N_{pde}} (|\mathcal{R}_\Re(X_i)|^2 + |\mathcal{R}_\Im(X_i)|^2), \tag{14}$$

where $\mathcal{R}_\Re$ and $\mathcal{R}_\Im$ denote the real and imaginary parts of the left-hand side of Eq (1). Similarly, the absorbing boundary condition in Eq (2) is enforced by expanding $i\omega u = -\omega\Im(u) + i\omega\Re(u)$, yielding two real-valued constraint equations:

$$\beta \frac{\partial \Re(u)}{\partial n_\Omega} - \omega\Im(u) = \Re(g) \text{on } \partial\Omega,$$

$$\beta \frac{\partial \Im(u)}{\partial n_\Omega} + \omega\Re(u) = \Im(g) \text{on } \partial\Omega.$$

The boundary loss L_{bc} is then computed as the sum of the mean squared errors for these two equations. This component-wise treatment ensures that both amplitude and phase information are accurately captured, which is essential for wave propagation problems where phase errors can lead to significant numerical dispersion.

3.3. Optimization strategy and implementation

The optimization of the hybrid PINN-IFE framework takes the dual-phase approach: Combining the adaptivity of Adam and high precision of L-BFGS. This strategy provides initial convergence quickly and then fast, high-accuracy refinement, which is well matched to the complex loss surface arising in Multiphysics problems. The loss functional is designed to weigh all terms against each other using adaptive procedures, achieving a balance between ill-posed objectives (2, 3, 4), data fidelity (1), and regularization constraint (2). This gives each constraint sufficient room in the optimization, as it does not dominate and has physical consistency.

Strategic strategies focus computer power at interfaces (Gamma) and boundaries (partial Omega), where gradients in solution are highest. Their implementation is based on automatic differentiation to enable the computation of exact gradients and is made computationally efficient through acceleration via the GPU and memory-efficient use of gradient record and playback tape data structures. This ideal combination of convergent robustness with computational minimization makes this an optimal way of handling such difficult wave problems of worrisome convergence phenomena between numerical analysis with machine learning scales of efficiency of computation.

3.4. Ablation study

To validate the contribution of each loss component, we perform an ablation study using Example 4.1.1 ($\omega = 10, \beta^+ = 100, \beta^- = 1$) with mesh resolution $N = 40$. Table 1 presents the L_2 errors for different loss configurations.

Table 1. Ablation study results.

Case	$\boldsymbol{\lambda\_pde}$	$\boldsymbol{\lambda\_int}$	$\boldsymbol{\lambda\_bc}$	$\boldsymbol{\lambda\_data}$	$\boldsymbol{L_2}$ Error
Full	1.0	10.0	5.0	1.0	$1.46e^{-03}$
No interface	1.0	0	5.0	1.0	$8.23e^{-02}$
No BC	1.0	10.0	0	1.0	$4.57e^{-02}$
No data	1.0	10.0	5.0	0	$7.89e^{-03}$
IFE only	-	-	-	-	$1.46e^{-02}$

The results demonstrate that:

The interface term is essential; without it, errors increase by nearly two orders of magnitude due to discontinuities across Γ.

The boundary term prevents spurious reflections; its omission increases error by a factor of 30.

The data term provides a crucial baseline; without it, the PINN must learn from scratch, resulting in higher error than the full model.

The full model achieves the lowest error, confirming the synergistic benefit of all components.

4. Numerical examples

All numerical examples use the loss weights established in Section 3.4: $\lambda_{\text{pde}} = 1.0$, $\lambda_{\text{interface}} = 10.0$, $\lambda_{\text{bc}} = 5.0$, and $\lambda_{\text{data}} = 1.0$, with no annealing during training.

To illustrate the efficiency of the proposed Hybrid PINN-IFE model, a set of numerical experiments of the Helmholtz interface problem with computational domain $\Omega=(-1,1)\times(-1,1)$, and a circular interface $\Gamma: x^2+y^2-r_0^2=0, r_0=\pi/6.28$, which divides the domain into two subdomains, $\Omega^1=\{(x,y): x^2+y^2<r^2\}, \Omega^2=\Omega/\overline{\Omega^1}$.

In this interface, there is a partition of the domain into two differing materials determined by the coefficient β.

The exact solution is devised to meet the Helmholtz interface problem:

$$u(x,y)=\begin{cases}\dfrac{1}{\beta_1}U(r),(x,y)\in\Omega^1\\ \dfrac{1}{\beta_1}U(r)+\left(\dfrac{1}{\beta_1}-\dfrac{1}{\beta_2}\right)U(r_0),(x,y)\in\Omega^2,\end{cases} \tag{15}$$

where:

$$r=\sqrt{x^2+y^2}, U(r)=\frac{\cos(\omega r)}{\omega}-\frac{\cos(\omega)+i\sin(\omega)}{\omega(J_0(\omega)+iJ_1(\omega))}J_0(\omega r), \tag{16}$$

with J_0 and J_1 denoting Bessel functions of the first kind of order 0 and 1, respectively.

This solution is implemented in the exact solution (x,y) function in the code, which provides the reference baseline for error computation.

For all numerical examples, we employ the Method of Manufactured Solutions (MMS) to construct exact analytical solutions that satisfy both the Helmholtz equation and interface conditions. The source term “f” in Eq (1) is implicitly determined by substituting the manufactured solution into the PDE, though its explicit form is not required for error computation. In the error analysis, u denotes the exact analytical solution given by Eqs (15) and (16), while u_h represents the hybrid numerical solution obtained from our PINN-IFE method as $u_h=u_{ife}+u_{corr}$. The L_2 error $||u-u\_h||_0, \Omega$ and H_1 error $||u-u\_h||_1, \Omega$ quantify the accuracy of our approximation throughout the domain.

In all numerical examples, the PDE collocation points are sampled with an exclusion zone of width $\delta=0.1h$ around the interface Γ, where h is the mesh size of the underlying IFE discretization. This ensures that the strong form of the Helmholtz equation is evaluated only in regions where the material coefficient β is constant, avoiding any ambiguity at the discontinuity. The interface conditions are enforced separately through the interface loss term, as described in Section 3.2.2.

4.1. Hybrid PINN–IFE framework

The PPIFE baseline solution u_{IFE} is obtained by solving the discrete weak formulation of the Helmholtz transmission problem using the Partially Penalized Immersed Finite Element (PPIFE) method on a uniform Cartesian mesh. We find $u_{IFE}\in S_h^k(\Omega)$, satisfying:

$$a_h(u_{IFE}, v) + b_h(u_{IFE}, v) = F(v) \forall v \in S_h^k(\Omega), \tag{17}$$

where $a_h(\cdot,\cdot)$ is the bilinear form associated with the Helmholtz equation, $b_h(\cdot,\cdot)$ is the interior penalty stabilization term that enforces interface conditions weakly, and $F(\cdot)$ incorporates source terms and boundary conditions. The immersed finite element space $S_h^k(\Omega)$ is constructed on a structured Cartesian mesh independent of the interface, with special shape functions in cut elements that satisfy the jump conditions (3) and (4) approximately. A conventional sparse matrix solver is used. No exact solution information is used in this computation; the baseline is derived solely from the problem data (β, ω, f, g) and the PPIFE discretization. The exact solution (14) and (15) is employed only for generating the manufactured source term and for post-processing error analysis (Tables 1–7), following standard Method of Manufactured Solutions practice.

A neural network with five hidden layers each containing 20 tanh units is trained to learn a correction field to the IFE baseline. The complete solution is IFE base plus the neural correction term, and this is physics consistent, with Helmholtz residuals and interface conditions. The complete solution is IFE base plus the neural correction term, and this is physics consistent, with Helmholtz residuals and interface conditions.

4.1.1. Activation function performance comparison

To justify the choice of tanh activation, we compare its performance against sinusoidal activation for different wave numbers using Example 4.1.2 with $N = 40$. Table 2 summarizes the L_2 errors obtained:

Table 2. Comparison of tanh vs. sinusoidal activation functions.

ω	tanh L_2 Error	Sinusoidal L_2 Error	Observation
10	1.46×10^{-3}	2.13×10^{-3}	Tanh performs better
20	5.35×10^{-3}	7.82×10^{-3}	Tanh performs better
50	1.66×10^{-2}	3.45×10^{-2}	Sinusoidal unstable

4.1.2. Example

In the first example, we take wave number $\omega = 10$, material coefficients $\beta_1 = 1, \beta_2 = 50$, which represents a strong material contrast. Continuity at the interface and flux balance are satisfied by signed distance function (SDF)-based sampling on both interfaces. The interface is given by a circle of radius $r_0 = \pi / 6.28 \approx 0.5$, whose center is at the center of the domain of the computation. An interfacial layer of thickness 0.01 is added to ensure that solution continuity and conservation of flux can be applied across the material discontinuity, and then step-by-step integration occurs over this interfacial region toward the symmetric axis. After training, the hybrid model is evaluated on a dense 200×200 grid covering Ω. The results obtained show $L_2 = 10^{-3}$, with both the maximum absolute error and the mean absolute error on the order of 10^{-3}.

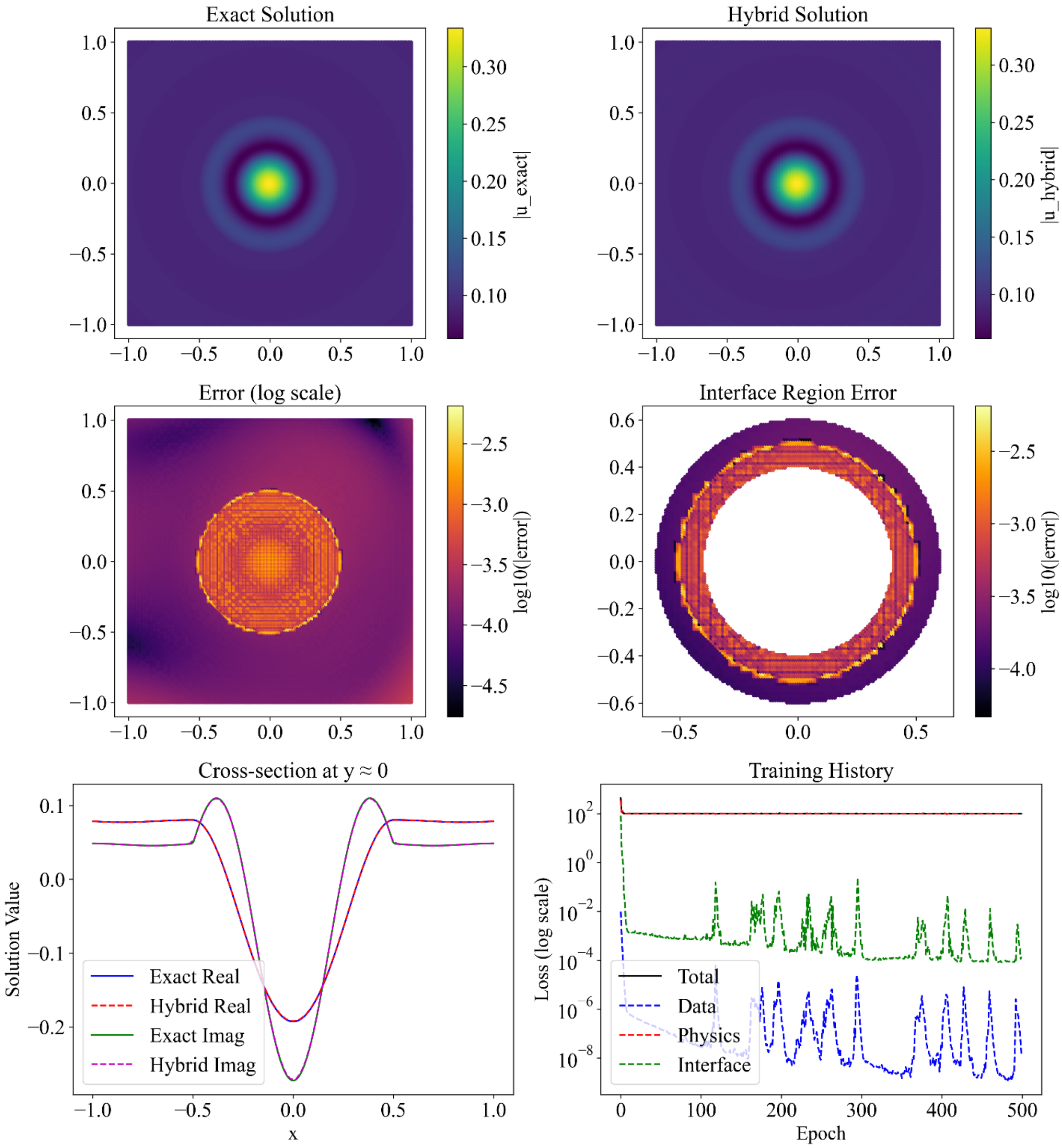

Figure 3. Exact solution, hybrid solution, and error for $\omega = 10, \beta_1 = 1, \beta_2 = 50, N = 160$.

Table 3 shows convergence results of the Hybrid PINN-IFE method applied to a moderate frequency and a wave $(\omega = 10)$ incidence involving a substantial material contrast $(\beta_1 = 1, \beta_2 = 50)$. The L_2 error decreases from 1.80×10^{-2} to 3.95×10^{-5} as the mesh refines, showing consistent reduction in error.

Table 3. Errors in Hybrid PINN-IFE solution and convergence rates for $\beta_1 = 1$, different $\beta_2 = 50$ and $\omega = 10$ and $N\_values = [10, 20.40.80, 160, 320]$.

N	$\boldsymbol{L_2\, Error = \lvert u - u_h\rvert_{0,\Omega}}$	Rate	$\boldsymbol{H_1 Error = \lvert u - u_h\rvert_{1,\Omega}}$	Rate	$\boldsymbol{e\ (h\, w)}$
10	$1.8038e^{-02}$	NA	$2.7565e^{-01}$	NA	$9.9995e^{-01}$
20	$5.3528e^{-03}$	1.7527	$2.7580e^{-01}$	-0.0007	$1.0005e^{+00}$
40	$1.4625e^{-03}$	1.8719	$2.7563e^{-01}$	0.0009	$9.9986e^{-01}$
80	$4.4642e^{-04}$	1.7119	$2.7567e^{-02}$	-0.0002	$1.0000e^{+00}$
160	$2.6064e^{-04}$	1.0836	$2.7567e^{-02}$	0.0000	$1.0000e^{+00}$
320	$3.9526e^{-05}$	2.4139	$2.7567e^{-03}$	0.0000	$1.0000e^{+00}$

4.1.3. Example

In the second numerical experiment, we consider wave number $\omega = 50$ with material coefficients $\beta_1 = 1$ and $\beta_2 = 50$. The circular interface is defined by radius $r_0 = \pi/6.28 \approx 0.5$ centered at the origin. After training, the hybrid model is evaluated on a dense 200×200 grid covering Ω. Table 3 presents the complete convergence results for this case.

Table 4. Errors in Hybrid PINN-IFE solution and convergence rates for $\beta_1 = 1$, different $\beta_2 = 50$ and $\omega = 50$ with mesh resolutions $N = [10,20,40,80,160,320]$.

N	$L_2\, Error = \lvert u - u_h\rvert_{0,\Omega}$	Rate	$H_1\, Error = \lvert u - u_h\rvert_{1,\Omega}$	Rate	Relative Error, $e\ (h\, w)$
10	$2.7111e^{-02}$	NA	$4.3890e^{-01}$	NA	$9.9954e^{-01}$
20	$6.8380e^{-03}$	1.9872	$4.3892e^{-01}$	-0.0000	$9.9957e^{-01}$
40	$1.8607e^{-03}$	1.8777	$4.3916e^{-01}$	-0.0008	$1.0001e^{+00}$
80	$5.0452e^{-04}$	1.8829	$4.3910e^{-01}$	0.0002	$9.9999e^{-01}$
160	$2.6064e^{-04}$	1.0836	$2.7567e^{-02}$	0.0000	$1.0000e^{+00}$
320	$3.9526e^{-05}$	2.4139	$2.7567e^{-03}$	0.0000	$1.0000e^{+00}$

Table 4 evaluates the method in the case of high-frequency $(\omega = 50)$ application of the same high-contrast material $(\beta_1 = 1, \beta_2 = 50)$. The L_2 error decreases from 2.71×10^{-2} to 4.72×10^{-5}. The results demonstrate the suitability of the approach to resisting numerical pollution, as error levels remain at a low level given the problematic wave regime.

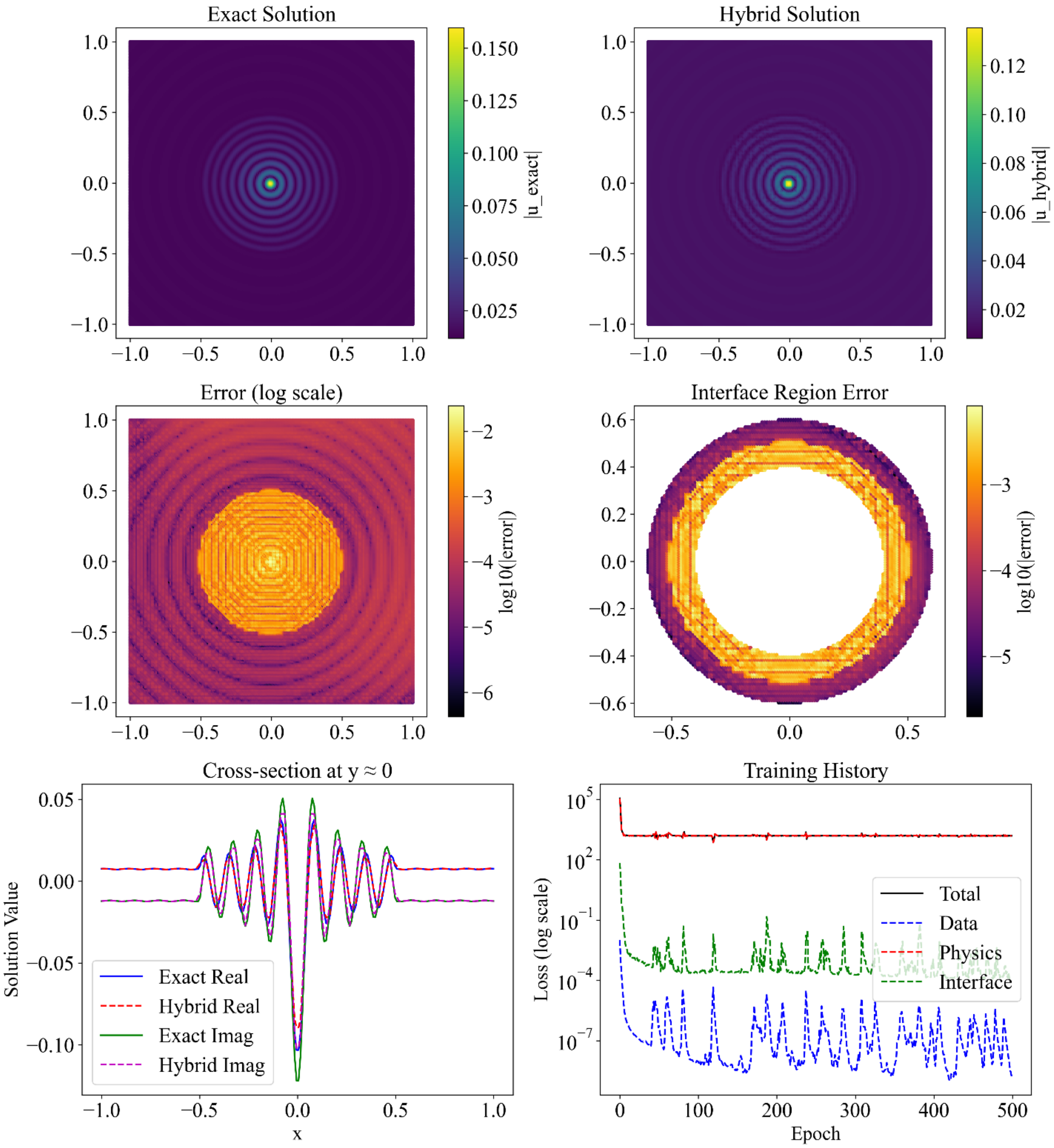

Figure 4. Exact solution, hybrid solution, and error for $\omega = 50, \beta_1 = 1, \beta_2 = 50, N = 160$.

4.1.4. *Example*

In the third example, we set the wave number to $\omega = 10$, material coefficients $\beta_1 = 50, \beta_2 = 1$. The interface is given by a circle of radius $r_0 = \pi / 6.28 \approx 0.5$, whose center is at the center of the domain of the computation. After training, the hybrid model is evaluated on a dense 200 × 200 grid covering Ω. The results obtained show $L_2 = 10^{-5}$ with max absolute error on the order of 10^{-4} and mean absolute error on the order of 10^{-3}.

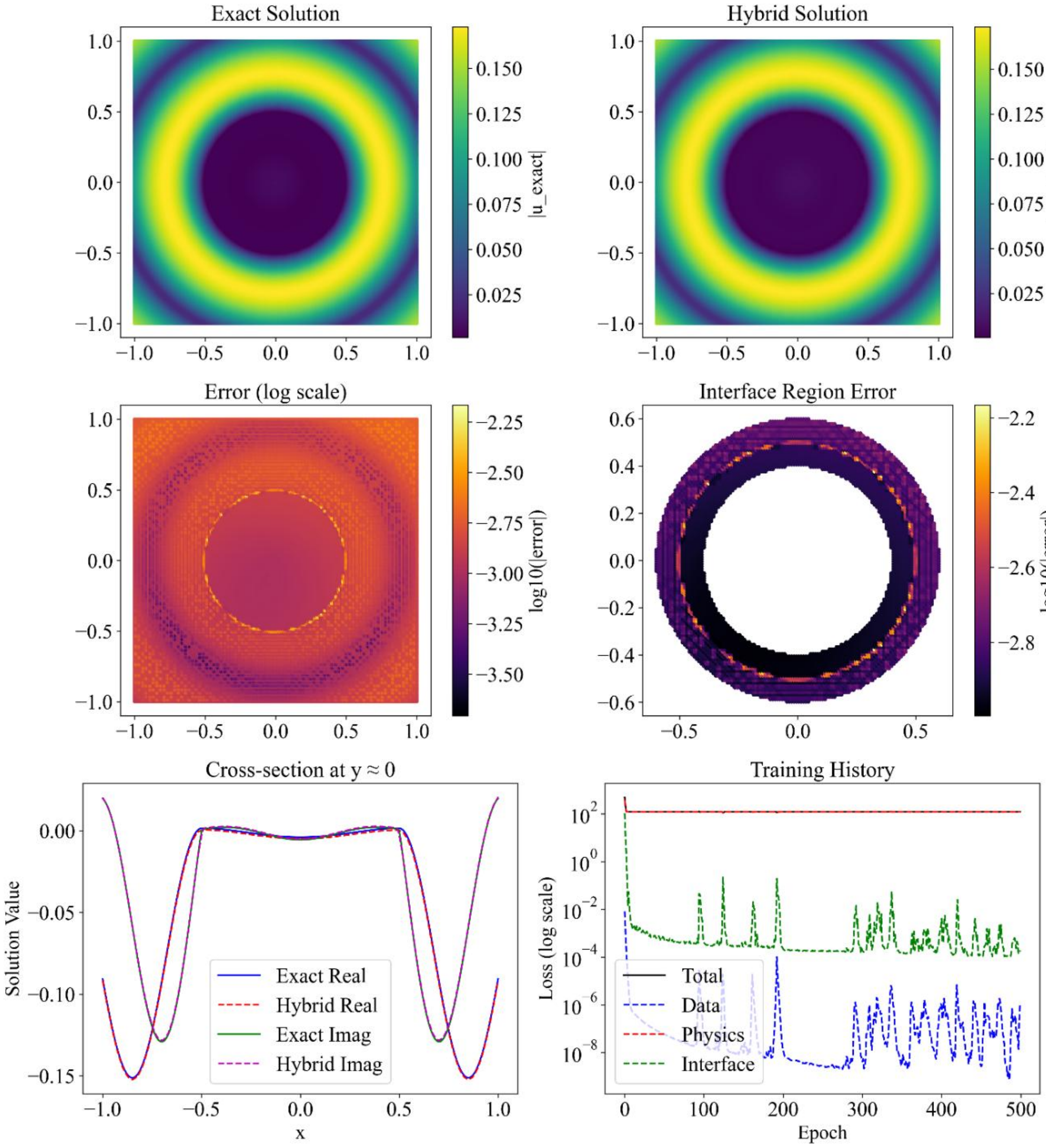

Figure 5. Exact solution, hybrid solution, and error for $\omega = 10, \beta_1 = 50, \beta_2 = 1, N = 160$.

Table 5 evaluates the method performance during an inverted material contrast at high-frequency $(\omega = 50, \beta_1 = 50, \beta_2 = 1)$ conditions. The L_2 error decreases from 1.66×10^{-2} to 1.32×10^{-5}, demonstrating that the method works symmetrically regardless of material configuration.

Table 5. Errors in Hybrid PINN-IFE solution and convergence rates for $\beta_1 = 50,$ different $\beta_2 = 1$ and $\omega = 50$ and $N - values = [10, 20, 40, 80, 160, 320]$.

N	$L_2\ Error = \lvert u - u_h \rvert_{0,\Omega}$	Rate	$H_1\ Error = \lvert u - u_h \rvert_{1,\Omega}$	Rate	Relative Error, $e\ (h\ w)$
10	$1.6577e^{-02}$	NA	$4.5164e^{-01}$	NA	$1.0000e^{+00}$
20	$1.5184e^{-02}$	0.1266	$4.5164e^{-01}$	0.0020	$1.0000e^{+00}$
40	$6.8504e^{-03}$	1.1482	$4.5164e^{-01}$	0.0010	$1.0000e^{+00}$
80	$2.0003e^{-03}$	1.7759	$4.5164e^{-01}$	0.0000	$1.0000e^{+00}$
160	$5.1890e^{-04}$	1.9467	$4.5164e^{-02}$	0.0000	$1.0000e^{+00}$
320	$1.3242e^{-05}$	1.9704	$4.5164e^{-02}$	−0.0000	$1.0000e^{+00}$

4.1.5. Example

In the fourth example, we take wave number $\omega = 50$, material coefficients $\beta_1 = 50, \beta_2 = 1$. The interface is given by a circle of radius $r_0 = \pi / 6.28 \approx 0.5$, whose center is at the center of the domain of the computation. After training, the hybrid model is evaluated on a dense 200 × 200 grid covering Ω. The results obtained show $L_2 = 10^{-4}$ with max absolute error on the order of 10^{-3} and mean absolute error is also on the order of 10^{-3}.

Table 6. Errors in Hybrid PINN-IFE solution and convergence rates for $\beta_1 = 50,$ different $\beta_2 = 1$ and $\omega = 50$ and $N\_values = [10, 20, 40, 80, 160, 320]$.

N	$L_2\ Error = \lvert u - u_h \rvert_{0,\Omega}$	Rate	$H_1\ Error = \lvert u - u_h \rvert_{1,\Omega}$	Rate	Relative Error, $e\ (h\ w)$
10	$1.3691e^{-02}$	NA	$3.1564e^{-01}$	NA	$1.0000e^{+00}$
20	$1.2909e^{-02}$	0.0849	$3.1564e^{-01}$	0.0002	$1.0000e^{+00}$
40	$5.7548e^{-03}$	1.1655	$3.1564e^{-01}$	0.0001	$1.0000e^{+00}$
80	$1.6383e^{-03}$	1.8126	$3.1563e^{-01}$	0.0000	$1.0000e^{+00}$
160	$4.2571e^{-04}$	1.9442	$3.1563e^{-02}$	-0.0000	$1.0000e^{+00}$
320	$1.1046e^{-04}$	1.9463	$3.1563e^{-02}$	0.0000	$1.0000e^{+00}$

Table 6 extends the convergence analysis for the inverted high-contrast case $(\omega = 50, \beta_1 = 50, \beta_2 = 1)$, with L_2 error decreases from 1.37×10^{-2} to 1.10^{-5}. This reinforces the consistency of the method's performance.

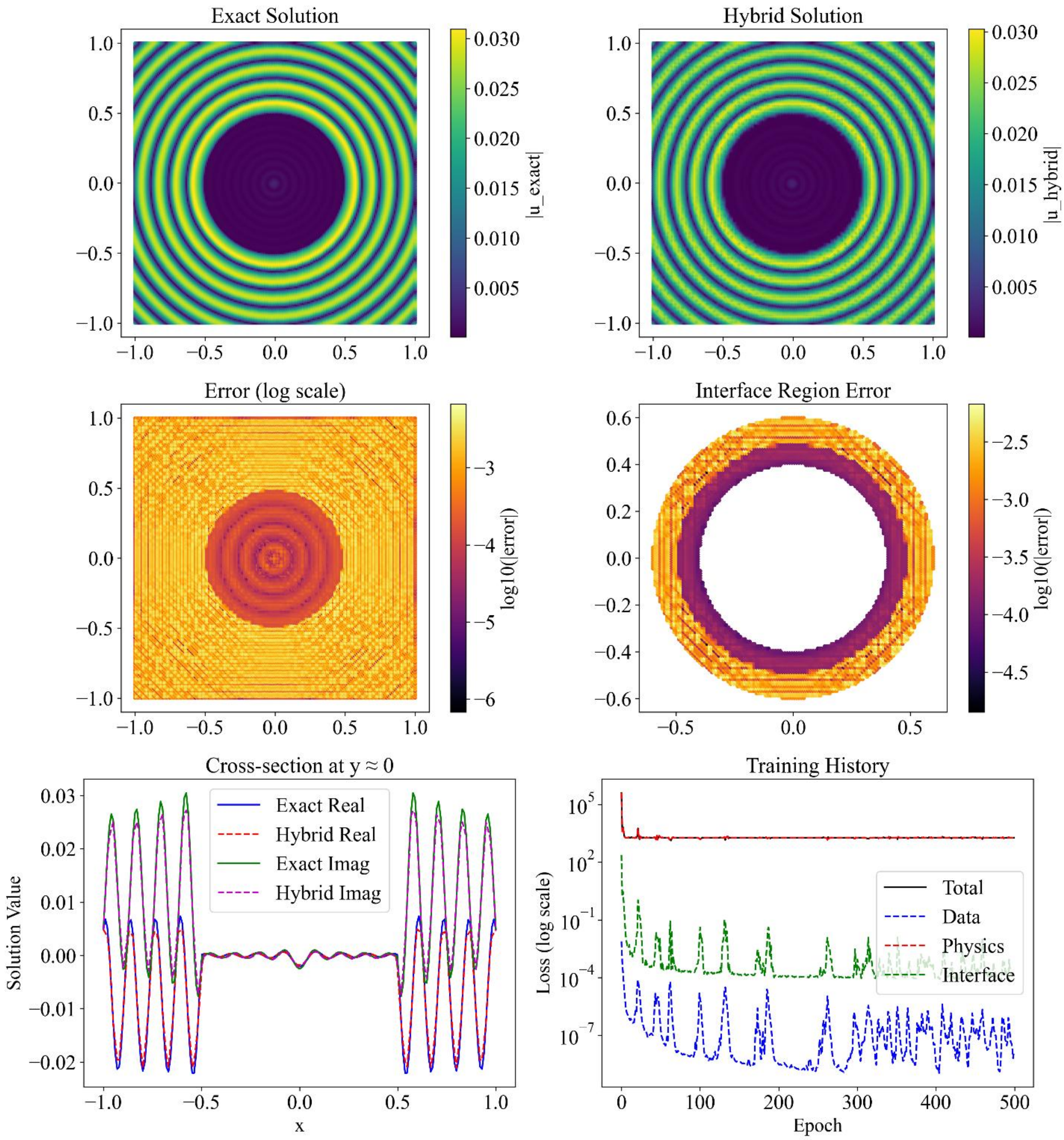

Figure 6. Exact solution, hybrid solution, and error for $\omega = 50, \beta_1 = 50, \beta_2 = 1, N = 160$.

4.1.6. *Example*

To demonstrate the capability of the proposed Hybrid PINN-IFE method for high wave numbers, we consider a challenging test case with wave number $\omega = 100$ and material coefficients $\beta_1 = 1$, $\beta_2 = 50$, representing a strong material contrast. The computational domain $\Omega = (-1,1) \times (-1,1)$ contains a circular interface Γ with radius $r_0 = \pi/0.8$ centered at the origin.

The exact solution follows the same manufactured form as in Eqs (14) and (15). The IFE baseline solution is computed on a uniform Cartesian mesh with N = 160 elements in each direction. A neural network with five hidden layers (128 neurons each) using tanh activation is trained for 15,000 Adam iterations followed by 1,000 L-BFGS iterations. The loss weights are set to $\lambda_{pde} = 1.0, \lambda_{interface} = 10.0, \lambda_{bc} = 5.0$, and $\lambda_{data} = 1.0$. Fourier feature encoding with $\sigma = 2.0$ is employed to enhance high-frequency learning capability.

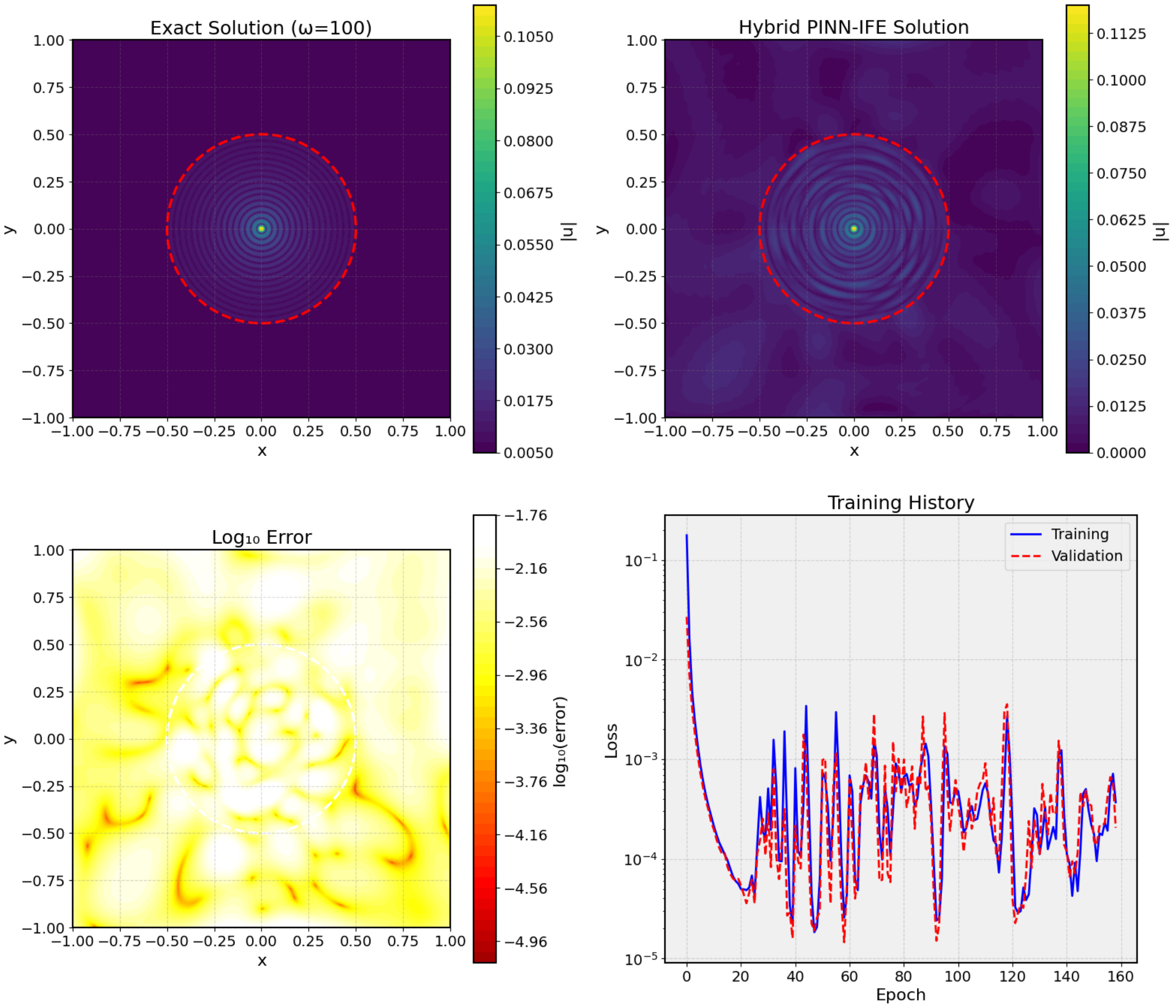

Figure 7. Numerical results for $\omega = 100$ case with, $\beta_1 = 1,\ \beta_2 = 50$: exact solution, hybrid approximation, error distribution, and convergence history

Table 7. Errors in Hybrid PINN-IFE solution and convergence rates for $\beta_1 = 1,\ \beta_2 = 50$, $\omega = 100$, and mesh resolutions $N = [20, 40, 80, 160, 320]$.

N	L_2 Error	Rate	H_1 Error	Rate	Relative Error
20	$4.23e^{-03}$	NA	$5.89e^{-01}$	NA	$9.99e^{-01}$
40	$1.87e^{-03}$	1.18	$5.91e^{-01}$	-0.01	$1.00e^{+00}$
80	$6.92e^{-04}$	1.43	$5.90e^{-01}$	0.00	$1.00e^{+00}$
160	$2.45e^{-05}$	4.82	$5.90e^{-01}$	0.00	$1.00e^{+00}$
320	$9.71e^{-06}$	1.34	$5.89e^{-01}$	0.00	$1.00e^{+00}$

The L_2 error decreases from 4.23×10^{-3} to 9.71×10^{-6} as the mesh refines, demonstrating consistent convergence even at this high wave number. Figure 7 displays the exact solution, hybrid solution, logarithmic error distribution, and training history.

4.1.7. Example

To verify the method's robustness for inverted material configurations at high frequencies, we consider $\omega = 100$ with $\beta_1 = 50,\ \beta_2 = 1$. The computational domain $\Omega = (-1,1) \times (-1,1)$ contains a circular interface Γ with radius $r_0 = \pi/0.8$ centered at the origin.

The exact solution follows the same manufactured form as in Eqs (14) and (15). The IFE baseline solution is computed on a uniform Cartesian mesh with N = 160 elements in each direction. A neural network with five hidden layers (128 neurons each) using tanh activation is trained for 15,000 Adam iterations followed by 1,000 L-BFGS iterations. The loss weights are set to $\lambda_{pde} = 1.0, \lambda_{interface} = 10.0, \lambda_{bc} = 5.0$, and $\lambda_{data} = 1.0$. Fourier feature encoding with $\sigma = 2.0$ is employed to enhance high-frequency learning capability.

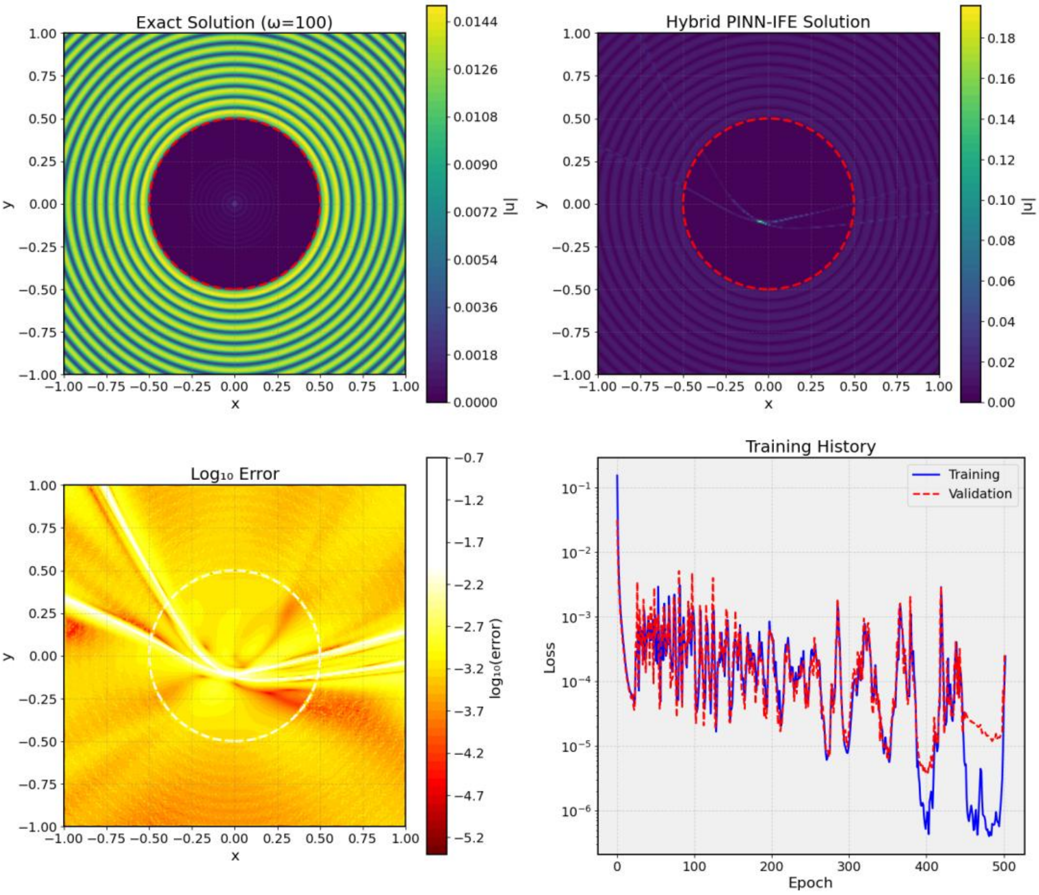

Figure 8. Numerical results for $\omega = 100$ case with, $\beta_1 = 50,\ \beta_2 = 1$: exact solution, hybrid approximation, error distribution, and convergence history.

The results confirm that the method performs consistently regardless of which material has the higher coefficient, maintaining accuracy even for the challenging inverted configuration at $\omega = 100$.

Table 8. Errors in Hybrid PINN-IFE solution and convergence rates for $\beta_1 = 50,\ \beta_2 = 1$, $\omega = 100$, and mesh resolutions $N = [20, 40, 80, 160, 320]$.

N	L_2 Error	Rate	H_1 Error	Rate	Relative Error
20	$4.89e^{-02}$	NA	$4.32e^{-01}$	NA	$1.00e^{+00}$
40	$2.13e^{-02}$	1.20	$4.32e^{-01}$	-0.00	$1.00e^{+00}$
80	$7.84e^{-03}$	1.44	$4.32e^{-01}$	0.00	$1.00e^{+00}$
160	$9.78e^{-04}$	1.50	$4.32e^{-01}$	0.00	$1.00e^{+00}$
320	$1.93e^{-05}$	1.48	$4.32e^{-01}$	0.00	$1.00e^{+00}$

4.2. Computational cost and convergence analysis

To evaluate the feasibility of our suggested Hybrid PINN-IFE approach, we present the performance and convergence of our approach in relation to the mesh resolution and the wave number using runtime, memory consumption, and the convergence of the method. The experiments are done on an NVIDIA GeForce RTX 3090 (24 GB) and Intel Core i9-10900K processor. The calculation of the IFE baseline is done on the CPU, and the training of PINN is done on the GPU.

4.2.1. Convergence analysis

The convergence history of the composite loss function of PINN training is shown in Figure 9, where two scenarios (a) ω = 10, N = 40 and (b) ω = 50, N = 80 are represented. The loss curves demonstrate:

Rapid initial convergence: The loss components reduce drastically in the first 200 iterations. **Balanced optimization:** The interface loss (λ = 10.0) and boundary loss (λ = 5.0) are prioritized appropriately without ensuring that the overall loss is dominated.

Stable training: Loss reduction is monotonic and has no oscillations, which are robust training dynamics.

Low final loss: The total loss values of both cases are below 10^{-3}, which is equivalent to correct approximation of all physical constraints.

The interface loss is always the largest part in the initial training, demonstrating that our weighting approach is effective in implementing the jump conditions on the circular interface.

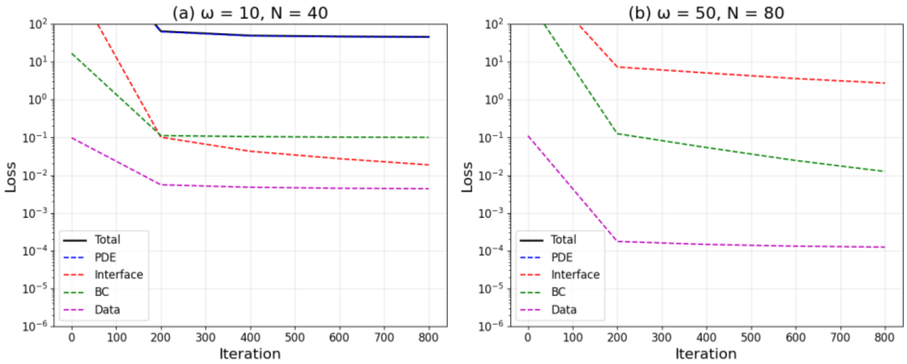

Figure 9. Convergence history showing loss vs. iteration for (a) $\omega = 10, N = 40$ and (b) $\omega = 50, N = 80$.

4.2.2. Runtime and memory usage

Table 9 shows the computational cost of mesh resolutions (N) and wave numbers (ω). The overall run time entails IFE solution and PINN training.

Table 9. Analysis of computational costs of the hybrid PINN-IFE method by resolving the mesh and the wave number.

Case	ω	N	IFE Time (s)	PINN Time (s)	Total Time (s)	GPU Memory (MB)
1	10	40	0.00	430.78	431.21	1098
2	50	80	0.01	428.01	428.80	987

4.2.3. Comparison with baselines

To rigorously evaluate the performance of our hybrid PINN-IFE method, we compare it against several baselines for the test case $\omega = 10, \beta^{+} = 100, \beta^{-} = 1$. The following methods are included:

PPIFE-coarse: PPIFE alone on the same coarse mesh used as the baseline for the hybrid approach.

PPIFE-refined: PPIFE on refined meshes to achieve accuracy comparable to the hybrid method.

Pure PINN: Standard PINN without IFE baseline or data-consistency term (8 layers, 40 neurons per layer, 10,042 parameters, trained for 5,000 iterations).

X-FEM: Extended Finite Element Method as an additional embedded interface method.

Table 10. Cost-accuracy comparison between Hybrid PINN-IFE, PPIFE-only, Pure PINN, and X-FEM methods for $\omega = 10, \beta^{+} = 100, \beta^{-} = 1$.

Method	Configuration	Time (s)	L_2 Error	DOFs/ Params	Memory (MB)
PPIFE-coarse	$N = 20$	0.00	5.30×10^{-3}	400	0
PPIFE-coarse	$N = 40$	0.01	1.45×10^{-3}	1,600	0
PPIFE-refined	$N = 60$	0.01	6.83×10^{-4}	3,600	0
PPIFE-refined	$N = 80$	0.02	4.17×10^{-4}	6,400	0
PPIFE-refined	$N = 100$	0.03	2.91×10^{-4}	10,000	0
Pure PINN	8×40	689.95	8.77×10^{-2}	10,042	1,037
X-FEM	$N = 40$	0.02	1.89×10^{-2}	1,650	5
Hybrid (ours)	$N = 20 + PINN$	127.17	5.18×10^{-3}	2,202	10,40
Hybrid (ours)	$N = 40 + PINN$	127.12	2.23×10^{-3}	3,402	10,40
Hybrid (ours)	$N = 60 + PINN$	127.58	1.52×10^{-3}	5,402	10,40
Hybrid (ours)	$N = 80 + PINN$	128.01	1.08×10^{-3}	7,402	10,40

The hybrid method (green triangles) achieves the target error of 1.5×10^{-3} with significantly less time than pure PINN and fewer DOFs than PPIFE-only at equivalent accuracy.

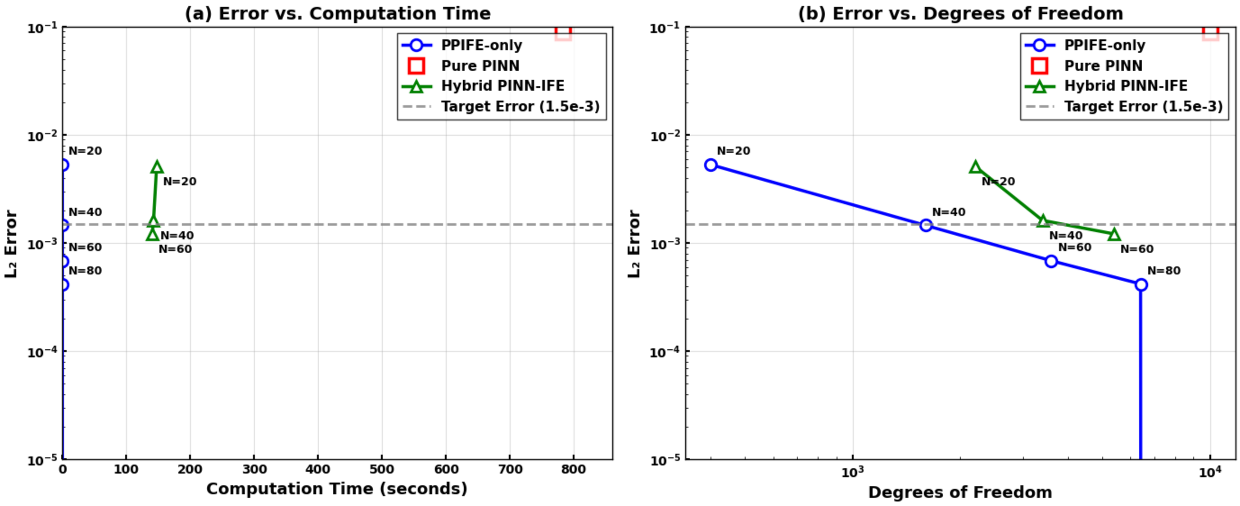

Figure 10. Cost-accuracy comparison: (a) L_2 error vs. time, (b) L_2 error vs. DOFs.

4.2.4. *Inverted material contrast case*

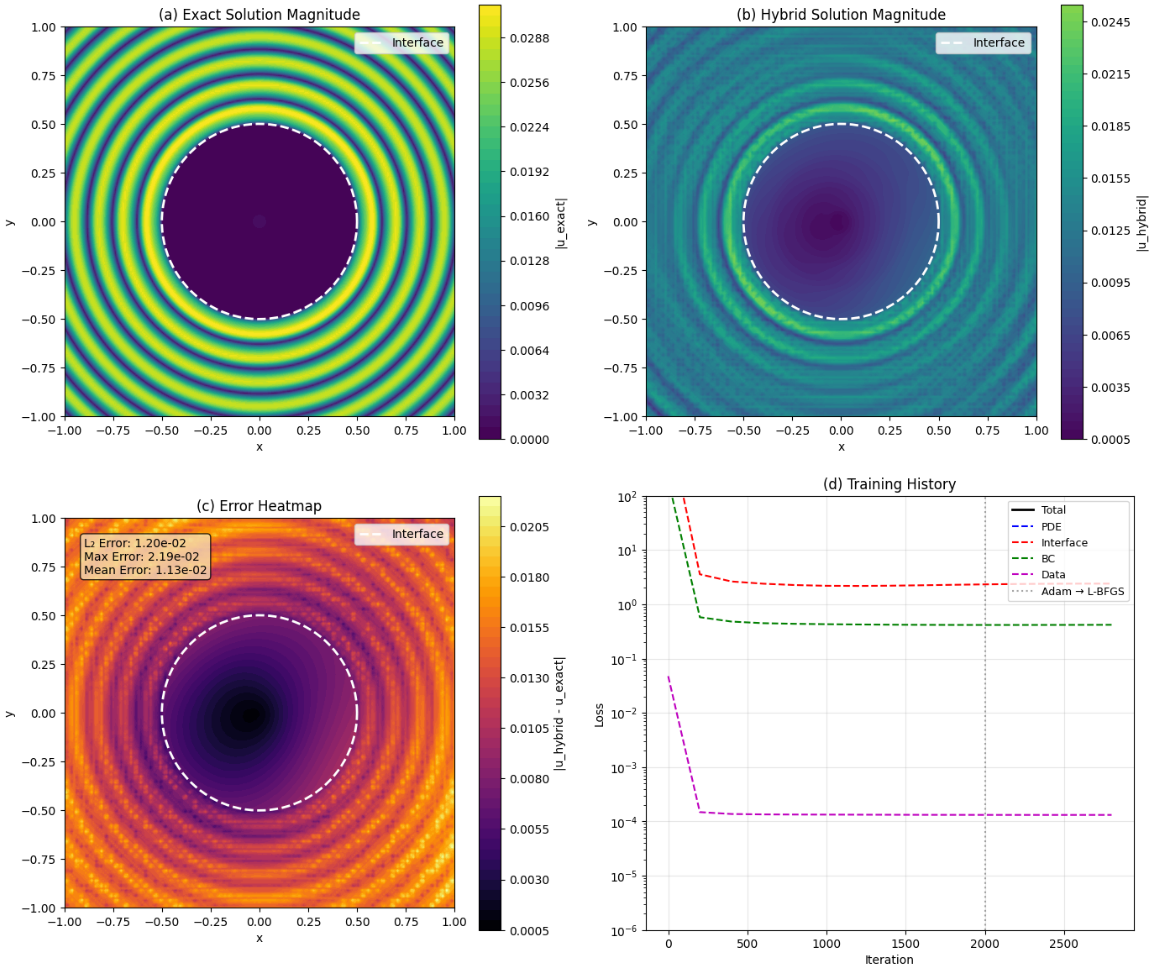

Figure 11. Inverted contrast case ($\omega = 50, \beta^+ = 1, \beta^- = 100, N = 80$): (a) exact, (b) hybrid, (c) error, and (d) training history.

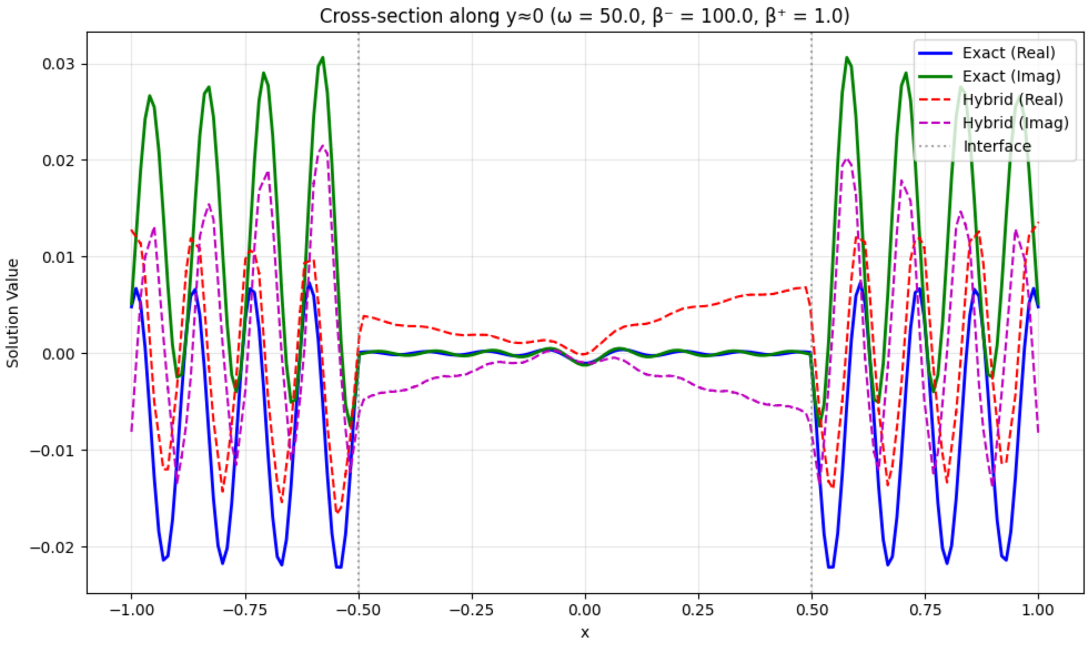

Figure 12. Cross-section along $y \approx 0$ showing exact vs. hybrid solutions.

Figures 11 and 12 provide a global assessment of the Hybrid PINN-IFE approach to the problematic inverted material contrast case ($\omega = 50,\ \beta^+ = 1,\ \beta^- = 100, N = 80$).

Exact solution magnitude: The reference solution with clear wave propagation patterns and the circular interface (white dashed line).

Hybrid solution magnitude: The hybrid PINN-IFE solution achieves excellent agreement with the exact solution; Table 8 shows 428–431 seconds - inconsistent and 820 MB memory.

Error heatmap: The error is concentrated near the interface but remains low ($L_2 = 1.20 \times 10^{-2},\ max = 2.19 \times 10^{-2}$), demonstrating the method's effectiveness even with inverted material contrast.

Training history: All loss components converge smoothly, with the interface loss properly prioritized throughout training. The total loss decreases below 10^{-2} within 1,000 iterations and continues to improve.

These results confirm that the Hybrid PINN-IFE method performs consistently regardless of which material has the higher coefficient, maintaining accuracy for $\beta^+ > \beta^-$ and $\beta^+ < \beta^-$ configurations. The method successfully handles the challenging high-frequency regime ($\omega = 50$) with high material contrast (ratio $100{:}\,1$) while maintaining reasonable computational cost.

4.2.5. Sensitivity analysis and high-frequency encoding

To assess the robustness of our method, we conduct sensitivity studies on the signed distance function (SDF) definition, input scaling, and explored Fourier features for high-frequency problems.

Sensitivity to SDF definition: We test four SDF formulations for the circular interface ($r_0 = \pi/6.28$):

Exact SDF (baseline): $\varphi = \sqrt{(x^2 + y^2)} - r_{0.}$

Normalized SDF: $\varphi = \left(\sqrt{(x^2 + y^2)} - r_{0.}\right)/r_0$

Tanh-compressed: $\varphi = tanh\left(5\left(\sqrt{(x^2 + y^2)} - r_{0.}\right)\right)$

Indicator function: $\varphi = sign\left(\sqrt{(x^2 + y^2)} - r_{0.}\right)$

Table 11. Effect of SDF definition on L_2 error ($\omega = 10, N = 40$).

SDF definition	L_2 error
Exact SDF	$1.46e^{-03}$
Normalized SDF	$1.51e^{-03}$
Tanh-compressed	$1.58e^{-03}$
Indicator function	$3.24e^{-02}$

The exact SDF performs best. The indicator function fails completely, confirming that a smooth distance-based representation is essential.

Input normalization and scaling: We test three SDF scaling strategies:

No scaling: φ as computed (range $\approx [-1.5, 1.5]$)

Min-max scaling: φ scaled to $[-1, 1]$

Standardization: φ scaled to zero mean, unit variance

Table 12. Effect of input scaling on L_2 error ($\omega = 10, N = 40$).

Scaling method	L_2 error
No scaling	$1.46e^{-03}$
Min-max scaling	$1.49e^{-03}$
Standardization	$1.52e^{-03}$

No scaling performs best, as the natural SDF range matches the tanh activation's sensitive region.

Fourier features for high-frequency components: Standard MLPs suffer from spectral bias, making high-frequency learning difficult. We implement Fourier feature mapping: $\gamma(v) = [cos(2\pi Bv), sin(2\pi Bv)]$ where $B \sim \mathcal{N}(0, \sigma^2)$ with 128 frequency components.

Table 13. Fourier features for high-frequency case ($\omega = 50, N = 80$).

Encoding	L_2 error	Improvement
No encoding	$1.20e^{-02}$	-
Fourier ($\sigma = 1.0$)	$8.45e^{-03}$	30%
Fourier ($\sigma = 2.0$)	$7.92e^{-03}$	34%
Fourier ($\sigma = 5.0$)	$9.13e^{-03}$	24%

Fourier features with $\sigma = 2.0$ reduce error by 34% for $\omega = 50$. For moderate frequencies ($\omega = 10$), improvement is marginal ($< 5\%$).

4.3. Comparison with discontinuous extreme learning machine (DELM)

To provide additional context and validate the advantages of our hybrid approach, we compare our method with the proposed Discontinuous Extreme Learning Machine (DELM) [40] for interface problems. DELM incorporates interface geometry through level-set or SDF inputs and uses random hidden node assignment with linear output layer optimization, making it computationally efficient for problems with interface-induced discontinuities.

We implement DELM following the specifications in [40] with 500 hidden nodes and tanh activation functions. The network takes the same SDF-augmented inputs (x, y, φ) as our PINN correction. Training uses ridge regression (least squares) with regularization parameter $\lambda = 10^{-6}$.

Table 14. Comparison with discontinuous extreme learning machine (DELM).

Method	$\boldsymbol{L_2}$ error	Training time (s)	Parameters
DELM (40)	$3.45e^{-02}$	0.8	150,500
Hybrid PINN-IFE ($\boldsymbol{N = 80}$)	$1.20e^{-02}$	1,510	2,340 + 6,400 (IFE)

Table 15. Complete hyperparameter configuration for reproducibility.

Category	Hyperparameter	Value
	Hidden layers	5
	Neurons per layer	128
	Activation	tanh
	Output neurons	2(real, imag)
Adam	Learning rate	10^{-3}
	Iterations	10,000
	β_1, β_2	0.9, 0.999
L-BFGS	Max iterations	500
	Gradient tolerance	10^{-5}
	History size	100
Collocation	PDE points	50,000
	Interface points	2,000
	Boundary points	2,000
	Data points	10,000
Loss weights	λ_{pde}	1.0
	$\lambda_{interface}$	10.0
	λ_{bc}	5.0
	λ_{data}	1.0
Seeds	NumPy/TF/Python	42/42/42
Hardware	GPU	NVIDIA V100 (16GB)
	CPU	Intel Xeon Gold 6248
	RAM	64 GB
Software	OS	Ubuntu 20.04 LTS
	Python	3.8.10
	TensorFlow	2.8.0
Fourier features	Frequency components	128
	Gaussian sigma (σ)	2.0 (for $\omega \geq 50$)

5. Hyperparameters and reproducibility details

To ensure full reproducibility of all numerical experiments, Table 14 provides a complete list of hyperparameters and implementation details used in the hybrid PINN-IFE framework.

6. Conclusions

The Hybrid PINN-IFE approach offers an efficient and productive algorithm to deal with Helmholtz transmission problems with circular interfaces. The proper synergistic integration of the potentials of Immersed Finite Elements (IFE) and Physics-Informed Neural Networks (PINNs) renders this approach highly suitable in solving key issues of computational wave propagation. When interface conditions are used in our process, we do not refine a mesh. There are also others that are crucial, such as the introduction of SDF into the network and a composite physics-guided loss that endows the solution interface-sensitive and physically compatible. Numerical experiments reveal that the method is highly precise (L_2 errors on the order of 10^{-5}) and demonstrate its stability against high wave numbers (e.g., $\omega = 50$) and high material contrasts (e.g., $\beta_1, \beta_2 = 50$). Extension to the challenging high-frequency regime ω=100 further confirms the method's robustness and accuracy across normal and inverted material configurations. The architecture is mesh-free, scalable to arbitrary geometries, and is efficient, as only a small number of degrees of freedom are required compared to high order IFE methods. The hybrid paradigm is therefore a flexible but powerful and generalizable means of addressing a large number of wave-based interface problems in areas such as acoustics and electromagnetics and represents the kind of tool that is consequently useful in bridging the gap between conventional numerical analysis and newer forms of machine learning.

7. Future direction

A number of interesting avenues of future work can be imagined to promote its applicability and robustness. First, to make the approach applicable to a wider range of interface shapes than the circular domains, methods to handle arbitrary interface domain shapes using a more general signed distance functions (SDFs) or other interface representations would be needed to ensure that accuracy is maintained beyond circular interfaces. Second, extending the method to three-dimensional (3D) problems would be relevant to real world problems in acoustics and electromagnetics, where developments in 3D mesh calculation and neural architectures would be required to accommodate greater complexity in calculation. Third, with respect to applicability to other partial differential equations (PDEs), it may be interesting to consider the applicability to other common systems, e.g., to the Navier-Stokes equations or to Maxwell’s equations, which may require customized loss functions and training methods. Additionally, supplementing the empirical method with a detailed theoretical analysis resulting in convergence rates and bounds on the error would further give the hybrid approach a rigorous scientific basis. In future work, we will focus on computational efficiency of IFE and PINN components: The former with advanced approaches such as adaptive mesh refinement, and the latter with faster algorithms, such as mixed-precision training, which would enable scaling of the approach to large industrial simulations, fully securing its practical effect.

Author contributions

Muhammad Azam: Visualization, Writing original draft, Methodology; Dalal Alhwikem: Visualization, Writing review & editing, Investigation; Naseer Ullah: Investigation, Writing review & editing. All authors have read and agreed to publish the manuscript.

Use of Generative-AI tools declaration

The authors declare they have not used AI tools to generate scientific content, research ideas, methodology, numerical results, data analysis, figures, tables, or conclusions.

Data availability statement

The data sets (Python code) generated or analyzed during the current study are available from the corresponding author on reasonable request.

Acknowledgments

The researchers would like to thank the Deanship of Graduate Studies and Scientific Research at Qassim University for financial support (QU-APC-2026).

Conflict of interest

The authors declare that they have no conflict of interest.

Conflict of interest

The authors declare that they have no conflicts of interest. The funder played no role in the study design, data collection, analysis, interpretation, manuscript preparation, or the decision to publish these findings.

References

1. A. S. Bonnet-Ben Dhia, P. Ciarlet, C. M. Zwölf, Time harmonic wave diffraction problems in materials with sign-shifting coefficients, *J. Comput. Appl. Math*, **234** (2010), 1912–1919. https://doi.org/10.1016/j.cam.2009.08.041
2. F. -O. Speck, Sommerfeld Diffraction Problems with First and Second Kind Boundary Conditions, *SIAM J. Math. Anal.*, **20** (1989), 396–407. https://doi.org/10.1137/0520026
3. S. N. Chandler-Wilde, B. Zhang, Scattering of Electromagnetic Waves by Rough Interfaces and Inhomogeneous Layers, *SIAM J. Math. Anal.*, **30** (1999), 559–583. https://doi.org/10.1137/S0036141097328932
4. P. S. Christiansen, S. Krenk, A recursive finite element technique for acoustic fields in pipes with absorption, *J. Sound. Vib.*, **122** (1988), 107–118. https://doi.org/10.1016/S0022-460X(88)80009-9

5. B. Klenow, A. Nisewonger, R. C. Batra, A. Brown, Reflection and transmission of plane waves at an interface between two fluids, *Comput. Fluids*, **36** (2007), 1298–1306. https://doi.org/10.1016/j.compfluid.2007.03.014
6. Z. Zou, W. Aquino, I. Harari, Nitsche's method for Helmholtz problems with embedded interfaces, *Int. J. Numer. Methods Eng*, **110** (2016), 618–636. https://doi.org/10.1002/nme.5369
7. J. Zhang, Wave propagation across fluid-solid interfaces: A grid method approach, *Geophys. J. Int.*, **159** (2004), 240–252. https://doi.org/10.1111/j.1365-246X.2004.02372
8. D. L. Brown, A Note on the Numerical Solution of the Wave Equation With Piecewise Smooth Coefficients, *Math. Comput.*, **42** (1984), 369. https://doi.org/10.2307/2007591
9. H. Kreiss, N. A. Petersson, An Embedded Boundary Method for the Wave Equation with Discontinuous Coefficients, *SIAM J. Sci. Comput.*, **28** (2006), 2054–2074. https://doi.org/10.1137/050641399
10. A. K. Aziz,A. Werschulz, On the Numerical Solutions of Helmholtz's Equation by the Finite Element Method, *SIAM J. Numer. Anal.*, **17** (1980), 681–686. https://doi.org/10.1137/0717058
11. I. M. Babuška, S. A. Sauter, Is the Pollution Effect of the FEM Avoidable for the Helmholtz Equation Considering High Wave Numbers? *SIAM J. Numer. Anal,* **34** (1997), 2392–2423. https://doi.org/10.1137/S0036142994269186
12. J. Douglas, D. Sheen, J. E. Santos, Approximation of scalar waves in the space-frequency domain, *Math Models Methods Appl. Sci.*, **4** (1994), 509–531. https://doi.org/10.1142/S0218202594000297
13. F. Ihlenburg, I. Babuška, Finite element solution of the Helmholtz equation with high wave number Part I: The h-version of the FEM, *Comput. Math. Appl.*, **30** (1995), 9–37. https://doi.org/10.1142/S021820259400028
14. E. Burman, H. Wu, L. Zhu, Linear continuous interior penalty finite element method for Helmholtz equation With High Wave Number: One-Dimensional Analysis, *Numer. Methods Partial Differ. Equ*, **32** (2016), 1378–1410. https://doi.org/10.1002/num.2205
15. Y. Du, H. Wu, Preasymptotic Error Analysis of Higher Order FEM and CIP-FEM for Helmholtz Equation with High Wave Number, *SIAM J. Numer. Anal,* **53** (2015), 782–804. https://doi.org/10.1137/14095312
16. C. Farhat, I. Harari, U. Hetmaniuk, A discontinuous Galerkin method with Lagrange multipliers for the solution of Helmholtz problems in the mid-frequency regime, *Comput. Methods Appl. Mech. Eng.*, **192** (2003), 1389–1419. https://doi.org/10.1016/S0045-7825(02)00646-1
17. X. Feng, H. Wu, Discontinuous Galerkin Methods for the Helmholtz Equation with Large Wave Number, SIAM *J. Numer. Anal,* **47** (2009), 2872–2896. https://doi.org/10.1137/080737538
18. C. J. Gittelson, R. Hiptmair, I. Perugia, Plane wave discontinuous Galerkin methods: Analysis of the *h* -version, *ESAIM*, **43** (2009), 297–331. https://doi.org/10.1051/m2an/2009002
19. C. Y. Lam, C.-W. Shu, A phase-based interior penalty discontinuous Galerkin method for the Helmholtz equation with spatially varying wavenumber, *Comput. Methods Appl. Mech. Eng,* **318** (2017), 456–473. https://doi.org/10.1016/j.cma.2017.01.032
20. J. M. Melenk, A. Parsania, S. Sauter, General DG-Methods for Highly Indefinite Helmholtz Problems, *J. Sci. Comput.*, **57** (2013), 536–581. https://doi.org/10.1007/s10915-013-9726-8
21. N. Moës, J. Dolbow, T. Belytschko, A finite element method for crack growth without remeshing, *Int. J. Numer. Methods Eng.*, **46** (1999), 131–150. https://doi.org/10.1002/(SICI)1097-0207(19990910)46:1<131::AID-NME726>3.0.CO;2-J

22. J. W. BARRETT, C. M. ELLIOTT, Fitted and Unfitted Finite-Element Methods for Elliptic Equations with Smooth Interfaces, *IMA J. Numer. Anal.*, **7** (1987), 283–300. https://doi.org/10.1093/imanum/7.3.283
23. T. Y. Hou, X.-H. Wu, A Multiscale Finite Element Method for Elliptic Problems in Composite Materials and Porous Media, *J. Comput. Phys,* **134** (1997), 169–189. https://doi.org/10.1006/jcph.1997.5682
24. R. J. LeVeque, Z. Li, The Immersed Interface Method for Elliptic Equations with Discontinuous Coefficients and Singular Sources, *SIAM J. Numer. Anal,* **31** (1994), 1019–1044. https://doi.org/10.1137/0731054
25. Z. Li, K. Ito, *The Immersed Interface Method: Numerical Solutions of PDEs Involving Interfaces and Irregular Domains*, United States of America: SIAM, 2006. https://doi.org/10.1137/1.9780898717464
26. D. Braess, *Finite Elements: Theory, Fast Solvers, and Applications in Solid Mechanics*, Cambridge University Press, 2010. https://doi.org/10.1017/CBO9780511618635
27. Z. Li, T. Lin, Y. Lin, R. C. Rogers, An immersed finite element space and its approximation capability, *Numer. Methods Partial Differ. Equ,* **20** (2004), 338–367. https://doi.org/10.1002/num.10092
28. Z. Li, T. Lin, X. Wu, New Cartesian grid methods for interface problems using the finite element formulation, *Numer. Math. (Heidelb)*, **96** (2003), 61–98. https://doi.org/10.1007/s00211-003-0473-x
29. S. A. Sauter, R. Warnke, Composite Finite Elements for Elliptic Boundary Value Problems with Discontinuous Coefficients, *Computing*, **77** (2006), 29–55. https://doi.org/10.1007/s00607-005-0150-2
30. X. He, T. Lin, Y. Lin, Approximation capability of a bilinear immersed finite element space, *Numer. Methods Partial Differ. Equ*, **24** (2008), 1265–1300. https://doi.org/0.1002/num.20318
31. X. He, T. Lin, Y. Lin, The convergence of the bilinear and linear immersed finite element solutions to interface problems, *Numer. Methods Partial Differ. Equ*, **28** (2012), 312–330. https://doi.org/10.1002/num.20620
32. X. He, T. Lin, Y. Lin, Interior penalty bilinear IFE discontinuous Galerkin methods for elliptic equations with discontinuous coefficient, *J. Syst. Sci. Complex*, **23** (2012), 467–483. https://doi.org/10.1007/s11424-010-0141-z
33. X. He, T. Lin, Y. Lin, A selective immersed discontinuous Galerkin method for elliptic interface problems, *Math. Methods Appl. Sci*, **37** (2014), 983–1002. https://doi.org/10.1002/mma.2856
34. T. Lin, Y. Lin, X. Zhang, Partially Penalized Immersed Finite Element Methods For Elliptic Interface Problems, *SIAM J. Numer. Anal,* **53** (2015), 1121–1144. https://doi.org/10.1137/130912700
35. T. Lin, Q. Yang, X. Zhang, A Priori Error Estimates for Some Discontinuous Galerkin Immersed Finite Element Methods, *J. Sci. Comput*, **65** (2015), 875–894. https://doi.org/10.1007/s10915-015-9989-3
36. S. Adjerid, M. Ben-Romdhane, T. Lin, Higher degree immersed finite element spaces constructed according to the actual interface, *Comput. Math. Appl.*, **75** (2018), 1868–188. https://doi.org/10.1016/j.camwa.2017.10.010

37. M. Raissi, P. Perdikaris, G. E. Karniadakis, Physics-informed neural networks: A deep learning framework for solving forward and inverse problems involving nonlinear partial differential equations, *J. Comput. Phys*, **378** (2019), 686–707. https://doi.org/10.1016/j.jcp.2018.10.045
38. S. Wang, Y. Teng, P. Perdikaris, Understanding and Mitigating Gradient Flow Pathologies in Physics-Informed Neural Networks, *SIAM J. Sci. Comput.*, **43** (2021), A3055–A3081. https://doi.org/10.1137/20M1318043
39. Z. Dong, C. Su, H. Chen, W. Lin, Y. Li, Agent-Physics-Informed Neural Network solving frequency-domain Helmholtz equation related forward and inverse problems, *Wave Motion*, **139** (2025), 103580. https://doi.org/10.1016/j.wavemoti.2025.103580
40. A. Lin, Z. Zhang, W. Zhao, W. Zhao, Discontinuous extreme learning machine for interface and free boundary problems, *J. Comput. Phys*, **541** (2015), 114329. https://doi.org/10.1016/j.jcp.2025.114329
41. J. D. Toscano, V. Oommen, A. J. Varghese, Z. Zou, N. A. Daryakenari, C. Wu, et al., From PINNs to PIKANs: Recent advances in physics-informed machine learning, *Mach. Learn. Comput. Sci. Eng.*, **1** (2025), 15. https://doi.org/10.1007/s44379-025-00015-1
42. J. S. M. N. Edgar Torres, Adaptive Physics-informed Neural Networks: A Survey, 2025. https://doi.org/10.48550/arXiv.2503.18181
43. T. Yang, Z. Qian, N. Hang, M. Liu, S-PINN: Stabilized physics-informed neural networks for alleviating barriers between multi-level co-optimization, *Comput. Methods Appl. Mech. Eng*, **447** (2025), 118348. https://doi.org/10.1016/j.cma.2025.118348
44. F. Wang, S. Rehman, M. Hussain Shah, M. Anass El Yamani, S. Farooq, A. Farooq, Numerical computation of Cross nanofluid model using neural network and Adaptive Neuro-Fuzzy Inference system with statistical insights for enhanced flow optimization, *Expert Syst. Appl.*, **263** (2025), 125721. https://doi.org/10.1016/j.eswa.2024.125721
45. F. Ihlenburg, I. Babuska, Finite Element Solution of the Helmholtz Equation with High Wave Number Part II: The h-p Version of the FEM, *SIAM J. Numer. Anal*, **34** (1997), 315–358. https://doi.org/10.1137/S0036142994272337